

Generation of the North Equatorial Undercurrent Jets by Triad Baroclinic Rossby Wave Interactions

BO QIU AND SHUIMING CHEN

Department of Oceanography, University of Hawai'i at Mānoa, Honolulu, Hawaii

HIDEHARU SASAKI

Earth Simulator Center, JAMSTEC, Yokohama, Japan

(Manuscript received 3 May 2013, in final form 26 August 2013)

ABSTRACT

Formation processes responsible for the North Equatorial Undercurrent (NEUC) jets that appear across the tropical North Pacific Ocean near 9°, 13°, and 18°N are explored both theoretically and using numerical models with different complexities. Analyses of an eddy-resolving global ocean general circulation model output reveal that the NEUC jets have a mode-1 baroclinic vertical structure and are spatially persistent on the interannual and longer time scales. This OGCM-simulated vertical structure prompts the authors to adopt the simpler, nonlinear 1½-layer reduced-gravity model, as well as the baroclinic Rossby wave triad interaction theory, to unravel the essential processes underlying the NEUC jets. The seed for the NEUC jets originates in annual baroclinic Rossby waves driven by the large-scale surface wind stress forcing. Emanating from the ocean basin's eastern boundary, these wind-forced "primary" waves are subject to nonlinear triad interactions and break down offshore where the e -folding time scale of the most unstable triad instability matches the advective time scale of the primary waves. The breakdown boundary of the wind-forced primary waves tends to tilt northeast–southwest and, west of this boundary, finite-amplitude eddies emerge, whose meridional scales are set by the most unstable short secondary waves participating in the triad interactions along the breakdown boundary. With their meridional scales set similarly by the short secondary waves, the time-mean zonal jets of characteristics resembling the observed NEUC jets are formed by the converging potential vorticity fluxes of these finite-amplitude eddies.

1. Introduction

With the advancement of satellite altimetry, our knowledge of the upper-ocean circulation variability has increased significantly over the past two decades. In comparison, information about the subthermocline circulation features remains fragmentary. In the tropical North Pacific Ocean of interest to this study (i.e., 8°–25°N), past in situ measurements have sporadically detected eastward flows beneath the wind-driven, westward-flowing, North Equatorial Current (NEC). For example, Toole et al. (1988) presented evidence for subthermocline eastward flows at 10° and 12°N from two hydrographic surveys along 130°E. Based on multiple hydrographic

cruises along the same longitude, Hu and Cui (1991) and Wang et al. (1998) observed subthermocline eastward flows at 12° and 18°N. A subthermocline eastward jet was identified to be a time-mean feature at ~10°N by Qiu and Joyce (1992) along 137°E based on long-term repeat hydrographic surveys in 1967–88. In the central Pacific Ocean between Hawaii and Tahiti, year-long repeat hydrographic surveys by Wyrki and Kilonsky (1984) have observed similar, multicored, eastward subthermocline flows beneath the surface-intensified NEC. In addition to these studies using the hydrographic data, existence of the subthermocline eastward flows is also evident in recent shipboard acoustic Doppler current profiler (ADCP) measurements. Examples of these can be found in Kashino et al. (2009) along 130°E and in Dutrieux (2009) along 130°, 137°, 145°, and 156°E, respectively.

The establishment of the International Argo Program in the early 2000s (Roemmich et al. 2009) now provides us with a novel in situ dataset to explore the middepth

Corresponding author address: Dr. Bo Qiu, Department of Oceanography, University of Hawaii at Manoa, 1000 Pope Road, Honolulu, HI 96822.
E-mail: bo@soest.hawaii.edu

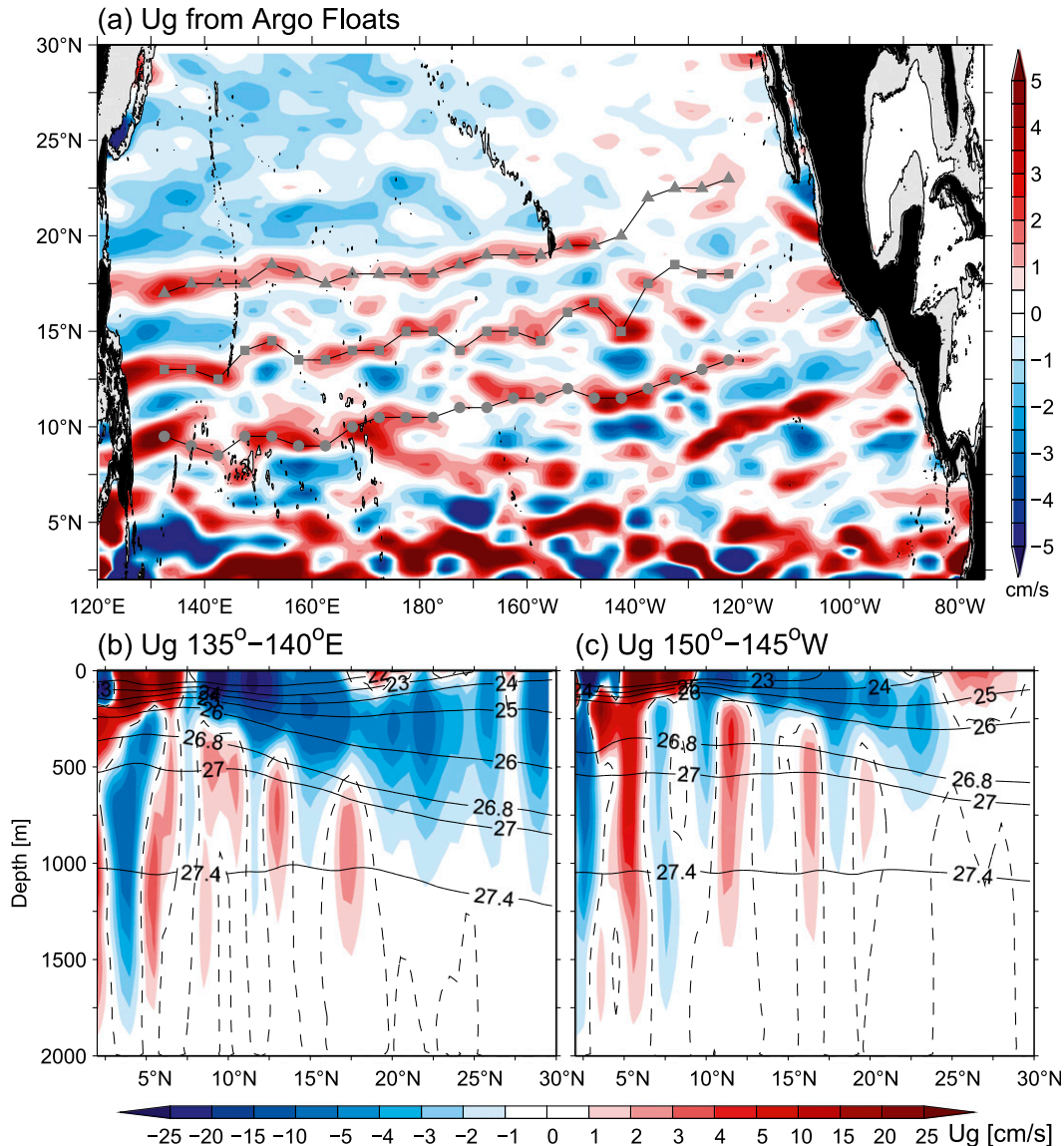


FIG. 1. (a) Distribution of zonal geostrophic velocity averaged between the $26.8\text{-}\sigma_\theta$ and $27.4\text{-}\sigma_\theta$ density surfaces from the Argo temperature/salinity data. Gray symbols denote the locations of the NEUC jet cores; see Qiu et al. (2013) for details. (b) Latitude–depth section of density (solid contours) and zonal geostrophic velocity (color shading) along $135^\circ\text{--}140^\circ\text{E}$. (c) As in (b), but for $150^\circ\text{--}145^\circ\text{W}$.

circulation features. Utilizing the drift information of consecutive float profiles, Cravatte et al. (2012) have constructed maps of the mean zonal flows in the $12^\circ\text{S}\text{--}12^\circ\text{N}$ band of the equatorial Pacific at the float parking depths of 1000 and 1500 m (see also Ascani et al. 2010). They found alternating westward and eastward jets with a meridional scale of $\sim 1.5^\circ$ and speeds of $\sim 5\text{ cm s}^{-1}$. The jets are generally stronger in the western and central basins and tend to weaken, or disappear, in the eastern basin. Similar equatorial zonal jets have been detected by Ollitrault et al. (2006) in the subthermocline Atlantic Ocean with the use of acoustic RAFOS float data.

By combining the profiling float temperature–salinity data from the International Argo and the Origins of the Kuroshio and Mindanao Current (OKMC) projects, Qiu et al. (2013) quantified recently the middepth mean flow structures across the entire tropical North Pacific basin within $2^\circ\text{--}30^\circ\text{N}$. As summarized in Fig. 1, three well-defined eastward jets are detected beneath the wind-driven, westward-flowing, NEC. Dubbed the North Equatorial Undercurrent (NEUC) jets, these subthermocline jets have a typical core velocity of $2\text{--}5\text{ cm s}^{-1}$ and are spatially coherent from the western boundary to about 120°W across the North Pacific basin.

Centered around 9°, 13°, and 18°N in the western basin, the NEUC jet cores tend to migrate northward by several degrees in the eastern basin. Vertically, the cores of the NEUC jets are observed to shoal to lighter density surfaces as they progress eastward.

Exploring the formation mechanisms for the off-equatorial, oceanic zonal jets has a long history and remains an area of active research [see Berloff et al. (2009); Kamenkovich et al. (2009) for reviews and extensive references]. One commonly adopted explanation for the zonal jet formation is the arrest of inverse energy cascade by barotropic Rossby waves in the two-dimensional turbulent ocean (Rhines 1975). Within this theoretical framework, the time-mean, alternating zonal jets are generated spontaneously by β -plane geostrophic turbulence, whose meridional scale is set by the Rhines arrest scale $L_{Rh} = \sqrt{2U_{rms}/\beta}$, where U_{rms} is the root-mean-squared (rms) eddy velocity and β the meridional gradient of the planetary vorticity. For the off-equatorial Pacific Ocean, several recent studies based on high-resolution ocean general circulation model (OGCM) simulations have hinted that the meridional scales of the simulated jets are consistent with L_{Rh} in certain regions (e.g., Nakano and Hasumi 2005; Maximenko et al. 2005; Richards et al. 2006).

It is worth emphasizing the NEC along 9°–18°N across the North Pacific basin is a band with relatively low mesoscale eddy activity [see, e.g., Plate 8 in Ducet et al. (2000)]. Dynamically, this is due to the resistance of the NEC system against baroclinic instability (Qiu 1999). With this low level of mesoscale eddy variability related to the intrinsic stability of the NEC, we seek in this study an alternative explanation for the formation of the observed NEUC jets shown in Fig. 1. Specifically, we demonstrate that the NEUC jets derive their energy from the nonlinear eddies generated by triad instability of the wind-forced annual baroclinic Rossby waves in the eastern tropical Pacific Ocean. Within this dynamical framework, the wind-forced annual baroclinic Rossby waves act as the energy-containing primary waves and the meridional scale of the resultant zonal jets is determined by the most unstable, short secondary waves that participate in the nonlinear triad interactions.

The paper is organized as follows. In section 2, we explore the dynamical features of the NEUC jets, such as their vertical structures and temporal persistence, using the output from a global eddy-resolving OGCM simulation. This exploration complements the NEUC jet descriptions based on the float observations and leads us to adopt in section 3 a simpler nonlinear 1½-layer reduced-gravity model to examine numerically the essential dynamical processes responsible for the NEUC jet formation. The numerical model results of section 3

are further clarified in section 4 in light of the triad interaction theory of baroclinic Rossby waves. Nonlinear rectification that forms the NEUC jets from eddies of the triad instability is quantified in section 5. Section 6 summarizes the outcomes from the present study.

2. The OFES simulations

To clarify the nature and formation mechanisms of the NEUC jets, we examine first the model results from a multidecadal hindcast run of the OGCM for the Earth Simulator (OFES) (Sasaki et al. 2008). In this section, we explore the model's realism in comparison with the float-inferred, subthermocline circulation patterns. After this comparison, we will utilize the OFES model output to examine the temporal changes in the NEUC jets. While difficult to extract from the observational data, the time-varying signals, as we will find in this section, are crucial in unraveling the mechanisms responsible for the NEUC jet formation.

The OFES model covers the global domain from 75°S to 75°N; it has an eddy-resolving horizontal resolution of 0.1° and 54 vertical levels. The model code is based on Modular Ocean Model, version 3 (MOM3), modified for optimal performance by the Earth Simulator of Japan. The model was spun up for 50 years with monthly climatological atmospheric forcing from the National Centers for Environmental Prediction–National Center for Atmospheric Research (NCEP–NCAR) reanalysis (Kistler et al. 2001). This climatological run was followed by a 62-yr hindcast integration for the period of 1950–2011 using the NCEP–NCAR reanalysis daily-mean forcing data. In our present study, the model output from the hindcast run was analyzed. For more details on the OFES model, such as its initial/boundary conditions and subgrid-scale eddy parameterizations, readers are referred to Nonaka et al. (2006).

Figure 2a shows the zonal velocity field on the 27.0- σ_θ density surface averaged in 2001–11 from the OFES hindcast run. This 11-yr duration overlaps with the period of the Argo float measurements, on which the zonal velocity field of Fig. 1a was based. The modeled zonal flow pattern compares favorably to the observed flow field, and this is particularly true for the three NEUC jets appearing along ~9°, ~13°, and ~18°N, respectively. Vertically, the modeled NEUC jets also exhibit features consistent with those detected in the observations. In the western North Pacific basin, for example, both Figs. 1b and 2b show that the NEUC jets exist below the 26.8- σ_θ surface. In addition, both modeled and observed NEUC jets reveal shoaling to a lighter density surface in the eastern North Pacific basin (cf. Figs. 1c and 2c). While existing in similar latitude bands, the modeled NEUC

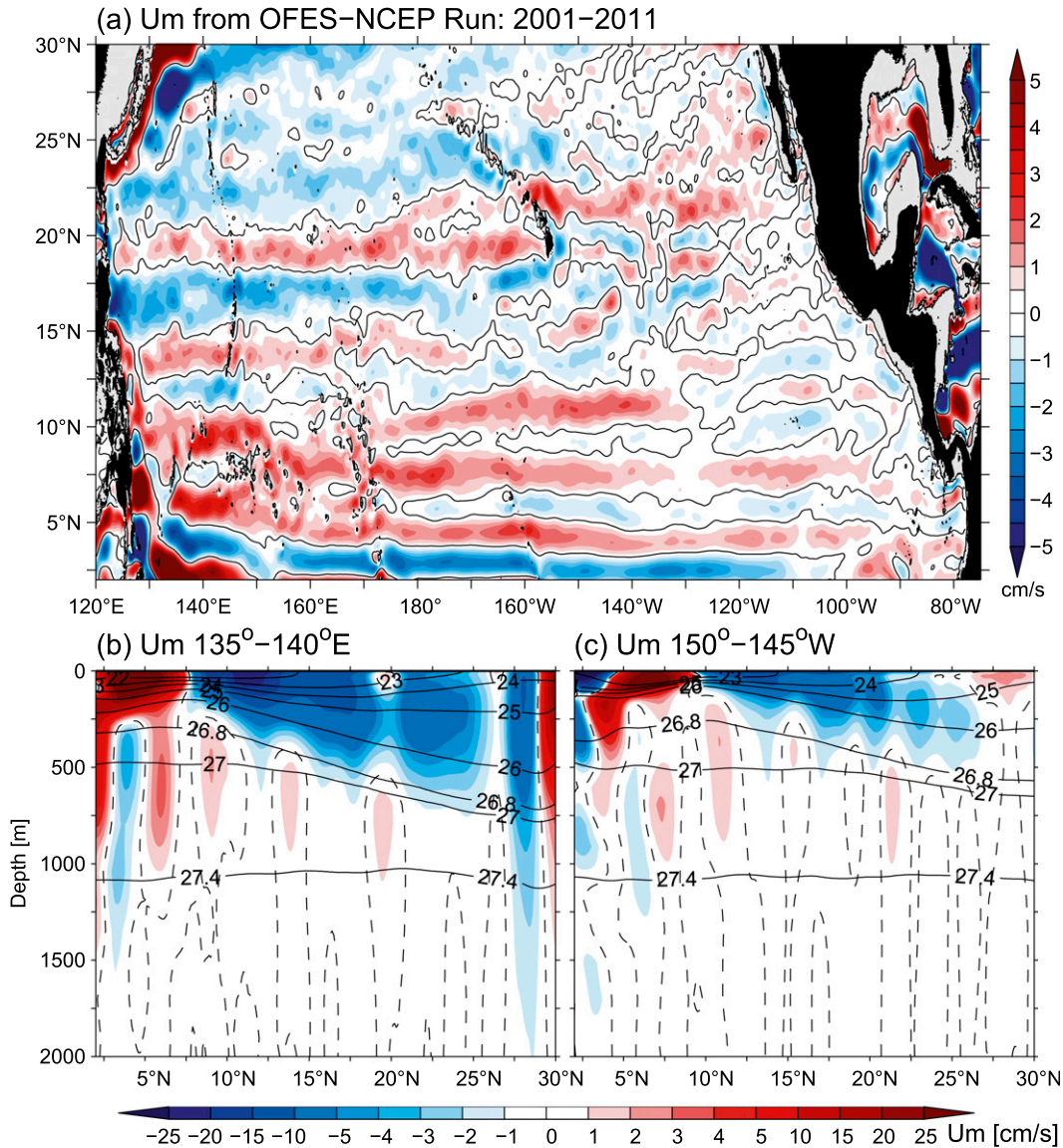


FIG. 2. (a) Distribution of zonal velocity on the 27.0- σ_θ density surface from the OFES simulation of 2001-11. (b) Latitude-depth section of density (solid contours) and zonal velocity (color shading) along 135°-140°E. (c) As in (b), but for 150°-145°W.

jets are, in general, 50% weaker in strength than those in the observations.

With the multidecadal OFES simulation results, it is possible to evaluate how persistently the three NEUC jets behave as the time-mean subthermocline features. To do so, we plot in Fig. 3 the zonal flows on the 27.0- σ_θ density surface averaged from 140°E to 170°W in the western North Pacific basin as a function of time and latitude. To focus on the time-mean signals, zonal flow variations shorter than 5 yr have been filtered out. While there exist low-frequency modulations in their intensities, the three NEUC jets remain, by and large, quasi

stationary along ~9°, ~13°, and ~18°N throughout the past six decades.

The modeled NEUC jets, however, do fluctuate on shorter time scales, and it is important from a dynamical viewpoint to elucidate the vertical structure of those fluctuations. To pursue this, we use the modeled $u(x, y, z = 600 \text{ m}, t)$ as a base time series and calculate its regression coefficient with the $u(x, y, z, t)$ time series at all other depths:

$$R(x, y, z) \equiv \frac{\langle u(x, y, z = 600 \text{ m}, t)u(x, y, z, t) \rangle}{\langle u^2(x, y, z = 600 \text{ m}, t) \rangle}, \quad (1)$$

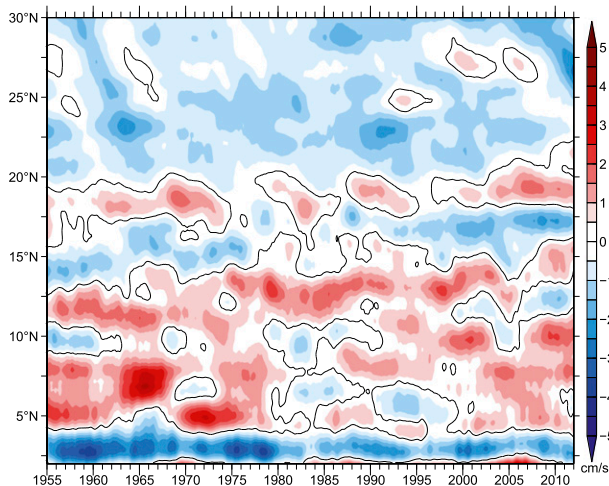


FIG. 3. Zonal velocity as a function of latitude and time on the $27.0\text{-}\sigma_\theta$ density surface averaged from 140°E to 170°W from the multidecadal OFES simulations. Flow variations shorter than 5 yr are filtered out.

where angle brackets denote the ensemble average over the period from 2001 to 2011. In Eq. (1), 600 m is chosen as the base depth because it represents the time-mean core depth of the NEUC jets. Figure 4a shows the regression coefficient $\bar{R}(z)$ spatially averaged in the $8^\circ\text{--}20^\circ\text{N}$, $130^\circ\text{E}\text{--}120^\circ\text{W}$ domain of the NEUC jets. The $\bar{R}(z)$ profile is clearly surface intensified and its vertical structure resembles the first baroclinic mode profile calculated using the regional stratification data—see Fig. 4b.¹ Dynamically, this OFES simulation result implies that the NEUC jets would have appeared above the main thermocline if it were not for the presence of the much stronger NEC driven by the large-scale surface wind stress curl forcing. Indeed, as shown in Fig. 5, if we remove the broad-scale zonal velocity signals by applying a 4° -box moving-average high-pass filter, the eastward NEUC jet signals in both the observations and the OFES simulation can now be seen to extend vertically to the surface and exhibit a modal structure similar to those presented in Fig. 4. In practice, this result indicates that the dynamics governing the NEUC jets can be sought in simple ocean models that capture the first baroclinic mode signals.

To examine the temporal variability of the modeled subthermocline circulation further, we plot in Fig. 6 the

¹ Following the recent theory of bottom pressure decoupling (e.g., Tailleux and McWilliams 2001), we derive the first baroclinic mode profile shown in Fig. 4b by solving the eigenvalue problem: $d[(f^2/N^2)d\Phi/dz]/dz - (\beta/c)\Phi = 0$, subject to $d\Phi/dz = 0$ at $z = 0$ and $\Phi = 0$ at $z = -H$. Here, $N^2 = -(g/\rho)d\rho/dz$ is squared buoyancy frequency and H is the depth of ocean bottom.

spatial map of rms velocity values on the $27.0\text{-}\sigma_\theta$ surface. As with Fig. 4, the 11-yr OFES model output from 2001 to 2011 was used to calculate the rms velocity values. Aside from the western boundary regions of island topography, an elevated rms velocity band appears in the $8^\circ\text{--}22^\circ\text{N}$ band that tilts from northeast to southwest. As will be detailed in section 4, this northeast–southwest tilting band is determined by the triad interaction of baroclinic Rossby waves.

Relating to Fig. 6, it is instructive to clarify the frequency content of the variability that gives rise to the rms velocity signals. In Fig. 7, we plot the x – t diagram of the $27.0\text{-}\sigma_\theta$ surface depth anomalies along 13°N (variability of similar nature occurs along other latitudes in the OFES simulations). Along 13°N , the time-varying depth signals undergo a transition around 135°W . East of this longitude, the anomalous depth signals are by and large dominated by annual-period variations. West of 135°W , on the other hand, the time-varying depth signals become more controlled by mesoscale eddies that possess shorter space–time scales. Reflecting the dominance of the first baroclinic mode dynamics, both the annual and mesoscale depth anomalies in Fig. 7 propagate westward at the first-mode baroclinic Rossby speed of $\sim 16.0\text{ cm s}^{-1}$ (e.g., Chelton et al. 2011). It is interesting to note that 135°W along 13°N is the location where the rms velocity value increases sharply from east to west in Fig. 6.

3. Zonal jets in a simplified Pacific Ocean model

Guided by the OFES simulation analyses revealing the dominance of the first baroclinic mode signals related to the NEUC jet variability, we adopt in this section a nonlinear $1\frac{1}{2}$ -layer reduced-gravity model to explore the jet formation mechanisms. Though simple in its dynamical formulations, the $1\frac{1}{2}$ -layer reduced-gravity model is capable of fully capturing the first baroclinic mode variability [see Qiu and Chen (2012) and references therein]. Using this model, we attempt to clarify the extent to which external parameters, such as eastern boundary geometry and surface wind forcing patterns, are relevant for the NEUC jet formations.

The equations governing the upper-ocean motion in the $1\frac{1}{2}$ -layer reduced-gravity system are

$$\frac{\partial \mathbf{u}}{\partial t} + \zeta \mathbf{k} \times \mathbf{u} = -\nabla E + A_h \nabla^2 \mathbf{u} + \frac{\boldsymbol{\tau}}{\rho_o H} \quad \text{and} \quad (2)$$

$$\frac{\partial H}{\partial t} + \nabla \cdot (H\mathbf{u}) = 0, \quad (3)$$

where $\zeta = f + \mathbf{k} \cdot \nabla \times \mathbf{u}$ denotes the absolute vorticity and $E = g'H + (u^2 + v^2)/2$ the total energy. In Eqs. (2)

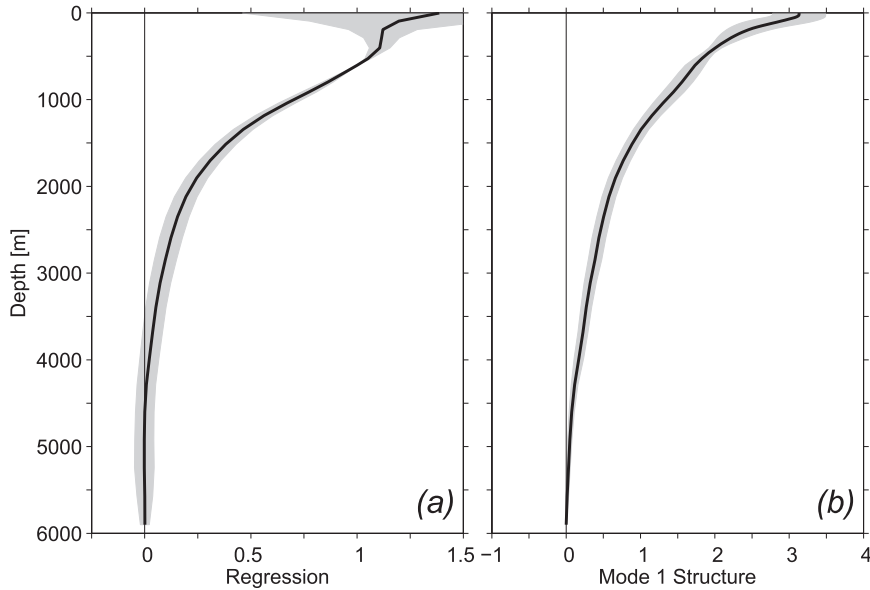


FIG. 4. (a) Regression coefficient of the OFES anomalous zonal velocities against those at the 600-m depth in the NEUC jet domain of 8°–20°N, 130°–120°W. (b) First baroclinic mode profile in the NEUC jet domain of 8°–20°N, 130°–120°W. In both plots, solid lines denote the domain-average values and shades denote the standard deviations. Based on the OFES model output of 2001–11.

and (3), $\mathbf{u} = (u, v)$ is the horizontal velocity vector, $\boldsymbol{\tau}$ the surface wind stress vector, H the time-varying upper-ocean-layer thickness, g' the reduced-gravity constant, ρ_o the reference density, and A_h the horizontal eddy viscosity coefficient. As the objective of our modeling work is to unravel the essential dynamics responsible for the NEUC jet formation, we start with our numerical experiment with the simplest possible model basin geometry: a box model of 50°S–50°N with a zonal width of 140° longitude. The size of the model mimics that of the whole Pacific Ocean. The model has a 0.25° grid resolution and an initial, uniform layer thickness $H_0 = 500$ m. The reduced-gravity constant is set at $g' = 0.018 \text{ m s}^{-2}$ so that the resultant phase speeds of the first-mode baroclinic Rossby waves match those observed in the Pacific Ocean (Chelton et al. 2011). The horizontal eddy viscosity coefficient $A_h = 20 \text{ m}^2 \text{ s}^{-1}$.

For simplicity, we force the model using the following idealized zonal wind stress:

$$\tau^x(y, t) = -W_0 \cos\left(\frac{\pi y}{L_y}\right) \cos(\omega_a t). \quad (4)$$

The forcing is x independent and modulates in time with an annual frequency $\omega_a = 2\pi/1 \text{ yr}$. Meridionally, $L_y = 40^\circ$ latitude, $y = 0$ is at the equator, and the $\cos(\pi y/L_y)$ term simulates the observed in-phase, large-scale, trade and westerly wind fluctuations in the tropical and

midlatitude Pacific oceans, respectively. The amplitude of τ^x , $W_0 = 0.042 \text{ N m}^{-2}$, is chosen to roughly represent the annual amplitude of the zonal wind stress forcing averaged over the Pacific Ocean. Notice that the time-mean wind forcing in Eq. (4) is zero and, as such, no Sverdrup tropical and subtropical gyres are formed in the modeled-mean circulation. This is done intentionally as we are interested in isolating the dynamics that are most relevant for the NEUC jet formation.

With the surface forcing specified by Eq. (4), we run the model for 30 years. Figure 8a shows the mean zonal velocity distribution averaged for the last 10 years during which the model flow field has reached a statistical equilibrium state (note that this distribution is robust and insensitive to the length of averaging period). Because of the symmetric forcing with respect to the equator, only the Northern Hemisphere model result is presented. Despite the zero time-mean wind forcing, Fig. 8a reveals that the modeled time-mean circulation is nonzero and dominated by alternating zonal jets with a meridional wavelength ~ 500 km. This wavelength compares well with that of the NEUC jets in the observations and the OFES simulation (Figs. 1 and 2). To gain further insight into the modeled alternating zonal jets, we plot in Fig. 8b a snapshot of the modeled upper-layer thickness (ULT) anomaly field. In the southeastern tropical region shown in Fig. 8b, the ULT anomalies clearly exhibit a sequence of annual baroclinic Rossby

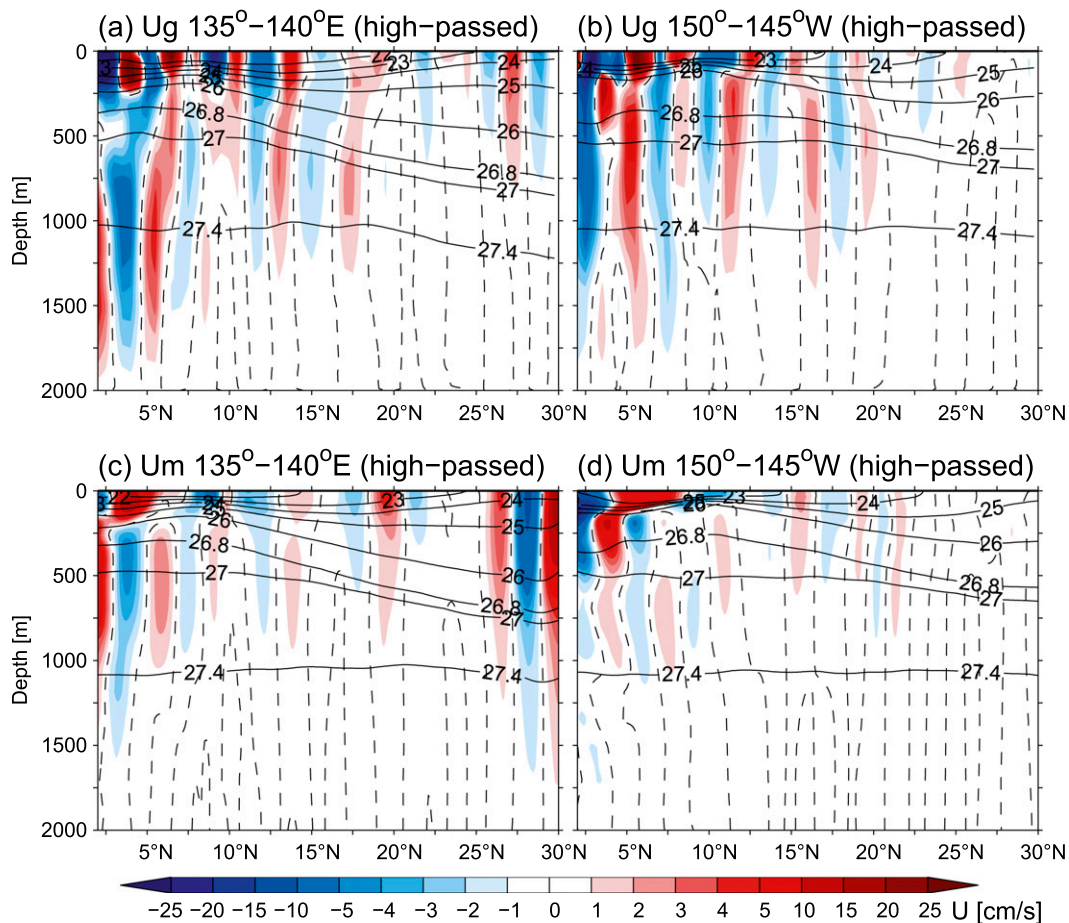


FIG. 5. Latitude–depth section of high-pass-filtered zonal geostrophic velocity (color shading) along (a) 135° – 140° E and (b) 150° – 145° W from the Argo temperature/salinity data. The high-pass filter removes signals using a 4° -box moving average. See Figs. 1b and 1c for the original velocity sections. (c),(d) As in (a) and (b), but for the zonal velocity from the OFES simulation. See Figs. 2b and 2c for the original velocity sections.

waves emanating from the eastern boundary. Because of their faster speed at lower latitudes, the cophase lines of the waves show the characteristic southwest–northeast tilting patterns. At some distance away from the eastern boundary, Fig. 8b reveals that the baroclinic Rossby waves start to break down, forming isolated mesoscale eddies. Farther to the west, the annual baroclinic Rossby wave signals are no longer discernable and the ULT anomaly field is populated with the westward-migrating break-off eddies.

This transition from the stable annual baroclinic Rossby waves to the irregular break-off eddies is demonstrated further in Fig. 9, in which we plot the ULT anomalies along 13° N as a function of longitude and time from the idealized model run. Notice that the transition along this latitude occurs about 40° west of the eastern boundary. Although less prominent than the signals presented in Fig. 9, a similar wave-to-eddy transition is detectable in Fig. 7 at a distance 40° west of the eastern

boundary in the OFES model simulation. This correspondence provides indirect evidence that the NEUC jets in the OFES simulation and our idealized model share the same generation mechanism, namely, the breakdown of the wind-driven annual baroclinic Rossby waves in the eastern Pacific basin.

To what extent do the zonal jet structures shown in Fig. 8a depend on the “unrealistic,” meridionally aligned eastern boundary assumed in our idealized model? To address this question, we replace the straight eastern boundary in the base model run with the realistic coastlines of the North and South America continents and repeat the 30-yr model integration. Figure 10 shows the results are in the same format as in Fig. 8 except from this “realistic eastern boundary” model run. While the details differ, the time-mean flow field in Fig. 10a is again dominated by the alternating zonal jets with a meridional wavelength of ~ 500 km. A similar transition from an annual Rossby wave–controlling eastern

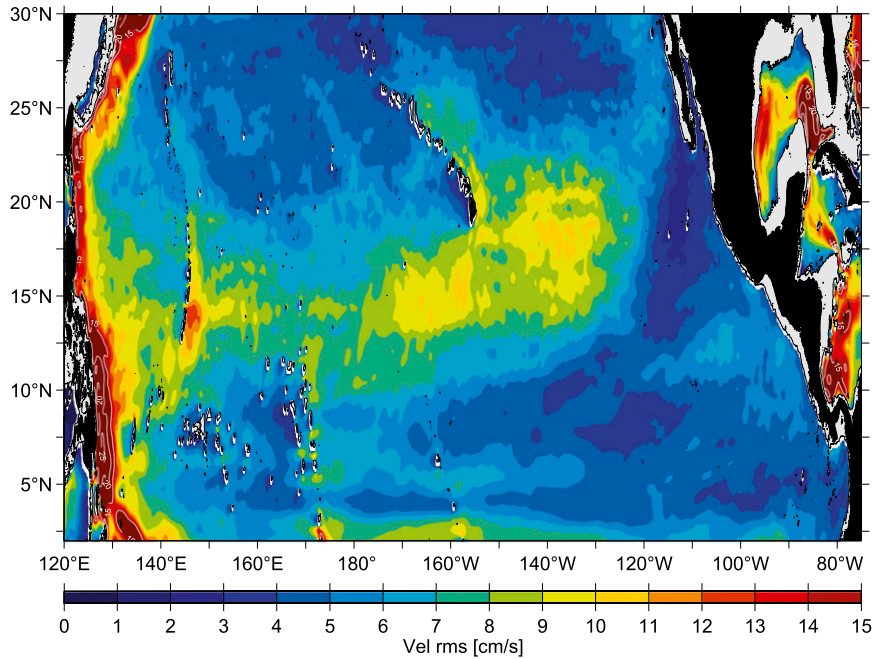


FIG. 6. Distribution of rms velocities on the 27.0- σ_θ density surface based on the OFES model output of 2001–11.

domain to an eddy-dominating western domain can be readily inferred from Fig. 10b. In other words, generation of the time-mean zonal jets with ~ 500 km wavelength is insensitive to the specific eastern boundary geometry adopted in our idealized model.

In the two model runs described above, we have used $A_h = 20 \text{ m}^2 \text{ s}^{-1}$ as the horizontal eddy viscosity coefficient. To examine how changing this coefficient may affect the modeled time-mean zonal jets, in particular their meridional scales, we repeat the base model runs with A_h increased to 100 and $200 \text{ m}^2 \text{ s}^{-1}$, respectively. Figure 11a shows the time-mean zonal flow pattern for the case $A_h = 100 \text{ m}^2 \text{ s}^{-1}$. Despite the fivefold increase in the A_h value, the time-mean zonal jets in Fig. 11a exhibit a meridional wavelength, ~ 500 km, similar to that shown in Fig. 8a. The strengths of the zonal jets, as may be expected, are generally weaker in Fig. 11a than in Fig. 8a. When A_h is further increased to $200 \text{ m}^2 \text{ s}^{-1}$, the modeled zonal jet strengths are reduced further, as shown in Fig. 11b (note that the color scale for Fig. 11b is half that for Fig. 11a). The meridional wavelength of the zonal jets, on the other hand, remains more or less the same as in the base case.

It is important to emphasize that the meridional wavelengths of the modeled zonal jets are sensitive to the amplitude of the external wind forcing. If we reduce the external wind forcing amplitude to $W_0 = 0.021 \text{ N m}^{-2}$ in Eq. (4) (i.e., half the amplitude of the base model run),

Fig. 12a shows that the meridional wavelength of the time-mean zonal jets in this case shortens to ~ 360 km, as compared to ~ 500 km in Fig. 8a. Relative to the base model run, the wave-to-eddy transition in this “half-amplitude forcing” run occurs at a distance farther to

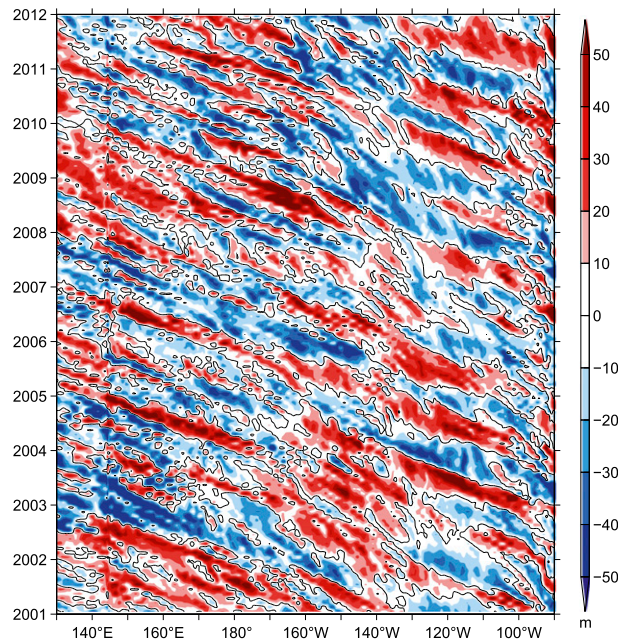


FIG. 7. Time–longitude diagram of the 27.0- σ_θ surface depth anomalies along 13°N from the OFES simulation.

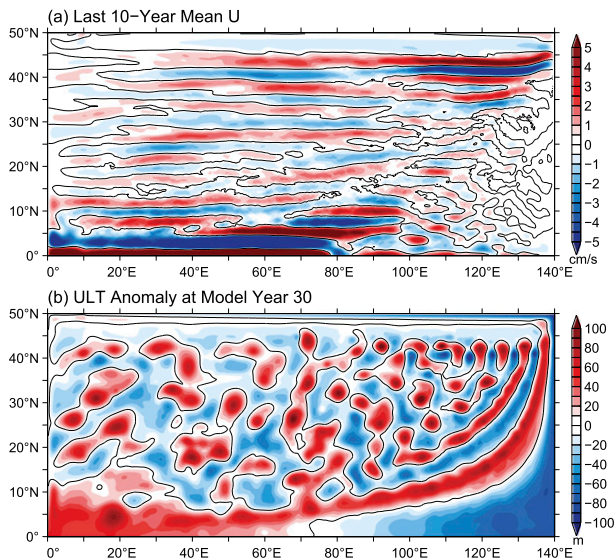


FIG. 8. (a) Distribution of time-mean zonal velocity from the base model run of the nonlinear $1\frac{1}{2}$ -layer reduced-gravity model. The time mean is taken from model year 20 to 30. (b) Snapshot of the base model's upper-layer thickness anomalies at year 30.0.

the west from the eastern boundary (instead of 40° in the base model run, for example, the transition in Fig. 12a occurs at 50° west of the eastern boundary along 13°N). When the external wind forcing amplitude is halved further to $W_0 = 0.0105 \text{ N m}^{-2}$, the meridional wavelength of the time-mean zonal jets is now only $\sim 280 \text{ km}$

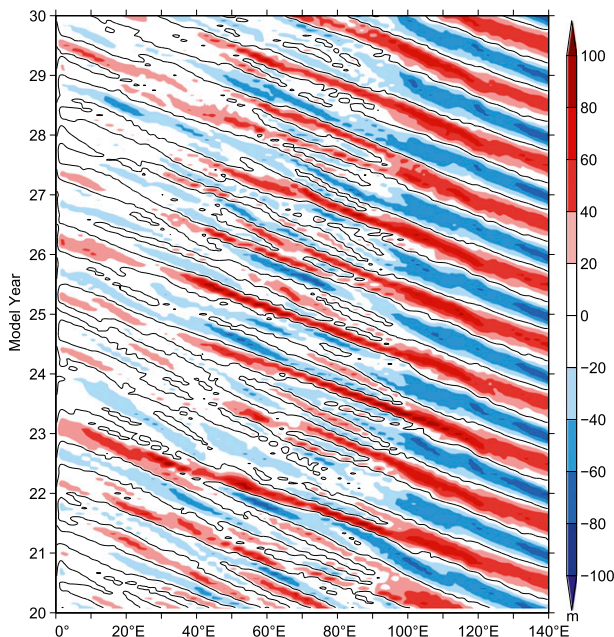


FIG. 9. Time-longitude diagram of the upper-layer thickness anomalies along 13°N from the nonlinear $1\frac{1}{2}$ -layer reduced-gravity base model run.

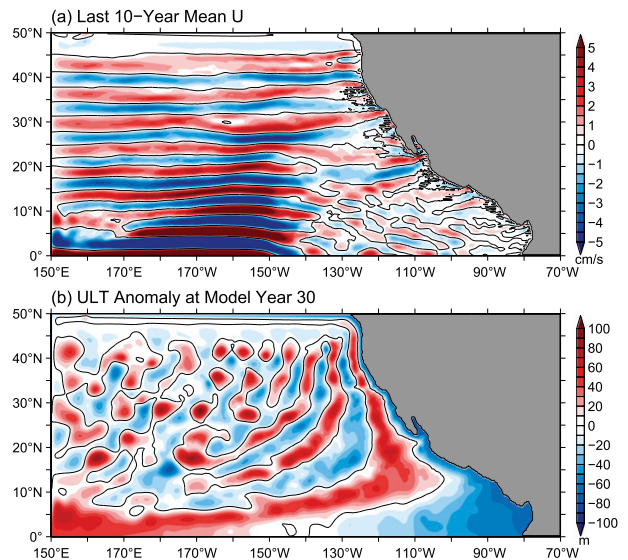


FIG. 10. (a) Distribution of time-mean zonal velocity from the nonlinear $1\frac{1}{2}$ -layer reduced-gravity model that has the realistic geometry of the America continents. All other model settings are the same as the base model run. (b) Snapshot of the model's upper-layer thickness anomalies at year 30.0.

(see Fig. 12b). In this “quarter-amplitude forcing” run, the location of wave-to-eddy transition also shifts farther to the west.

Questions such as how the eddy viscosity coefficient and external wind forcing amplitude control the meridional

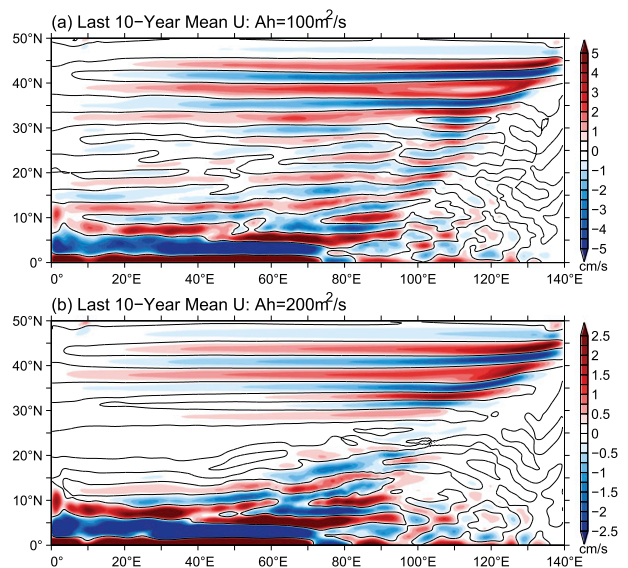


FIG. 11. (a) Distribution of time-mean zonal velocity from the nonlinear $1\frac{1}{2}$ -layer reduced-gravity model that has an increased horizontal eddy viscosity coefficient $A_h = 100 \text{ m}^2 \text{ s}^{-1}$. All other model settings are the same as the base model run. (b) As in (a), but for A_h increased further to $200 \text{ m}^2 \text{ s}^{-1}$.

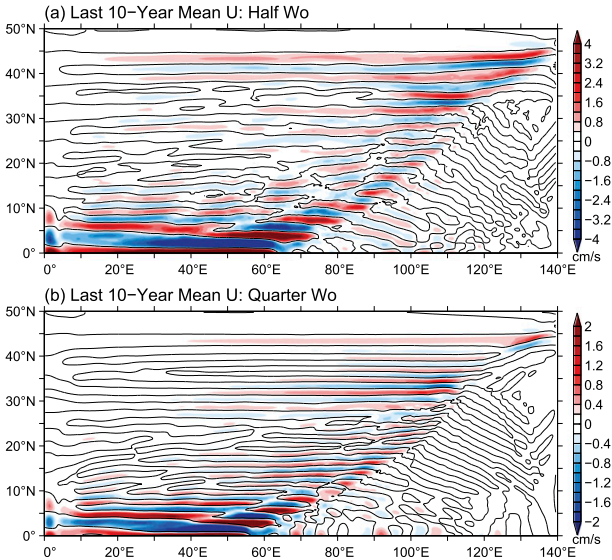


FIG. 12. (a) Distribution of time-mean zonal velocity from the nonlinear 1½-layer reduced-gravity model that has a reduced wind forcing amplitude $W_0 = 0.021 \text{ N m}^{-2}$, half of that in the base model run. All other model settings are the same as the base model run. (b) As in (a), but for W_0 further halved to 0.0105 N m^{-2} .

scales of the modeled zonal jets are addressed quantitatively in the next section when we explore the jet formation mechanisms from a theoretical point of view.

4. Resonant interaction of annual baroclinic Rossby waves

The analyses of both the state-of-the-art and simplified ocean model results in the preceding sections indicate that the NEUC jets are initiated by the breakdown of wind-driven annual baroclinic Rossby waves emanating from the eastern boundary. To better understand the nature of this breakdown, in particular to determine how the amplitude of the wind-driven annual baroclinic Rossby waves controls the meridional wavelength of the resultant zonal jets, we explore in this section the nonlinear interactions of the baroclinic Rossby waves within the framework of quasigeostrophic (QG) potential vorticity dynamics (Pedlosky 1987).

By adopting the β -plane approximation $f = f_0 + \beta y$ and defining the QG streamfunction $\psi = gH/f$, we can combine Eqs. (1) and (2) into the following QG potential vorticity equation in the unforced and nondissipative limit:

$$\frac{\partial}{\partial t} (\nabla^2 \psi - F\psi) + J(\psi, \nabla^2 \psi) + \beta \frac{\partial \psi}{\partial x} = 0, \tag{5}$$

where $F = f^2/g'H_0$ (or $1/L_d^2$) is reciprocal of the square of the baroclinic deformation radius L_d , and J is the

Jacobian operator. For the wind-driven annual baroclinic Rossby waves with $\psi \propto \exp i(kx + ly - \omega t)$, Eq. (5) requires that their frequency ω and wave-numbers (k, l) satisfy the dispersion relation:

$$\omega = -\frac{\beta k}{k^2 + l^2 + F}. \tag{6}$$

As detailed in Pedlosky (1987, section 3.26), although a monochromatic annual baroclinic Rossby wave is an exact solution to Eq. (5), a superposition of the baroclinic Rossby waves is not. Using the method of multiple time scales, we can expand ψ in terms of the small Rossby number $\epsilon \equiv U/\beta L^2$:

$$\psi = \psi_0 + \epsilon \psi_1 + \epsilon^2 \psi_2 + \dots, \tag{7}$$

where U and L are the characteristic particle velocity and length scale of the waves, respectively. At $O(1)$, ψ_0 satisfy the linearized Eq. (5), and it is instructive to assume it comprises three baroclinic waves:

$$\psi_0 = \sum_{j=1}^3 a_j \cos \theta_j, \tag{8}$$

where a_j is the wave amplitude, $\theta_j = k_j x + l_j y - \omega_j t + \phi_j$ with ϕ_j being an arbitrary phase angle, and each trio of (k_j, l_j, ω_j) satisfies the dispersion relation Eq. (6).

At the next $O(\epsilon)$, Eq. (5) becomes

$$\begin{aligned} \frac{\partial}{\partial t} (\nabla^2 \psi_1 - F\psi_1) + \beta \frac{\partial \psi_1}{\partial x} &= -J(\psi_0, \nabla^2 \psi_0) \\ &= \sum_{m=1}^3 \sum_{n=1}^3 \frac{a_m a_n}{2} B(K_m, K_n) [\cos(\theta_m + \theta_n) \\ &\quad - \cos(\theta_m - \theta_n)], \end{aligned} \tag{9}$$

where the interaction coefficient $B(K_m, K_n) = (K_m^2 - K_n^2)(k_m l_n - k_n l_m)$, $K_m^2 = k_m^2 + l_m^2$, and $K_n^2 = k_n^2 + l_n^2$. The rhs of Eq. (9) signifies that the nonlinear interactions among the three waves and their interaction becomes resonant if the following triad conditions are satisfied:

$$\begin{aligned} k_1 + k_2 + k_3 = 0; \quad l_1 + l_2 + l_3 = 0 \quad \text{and} \\ \frac{k_1}{k_1^2 + l_1^2 + F} + \frac{k_2}{k_2^2 + l_2^2 + F} + \frac{k_3}{k_3^2 + l_3^2 + F} \end{aligned} \tag{10}$$

The last, above condition is derivable from $\omega_1 + \omega_2 + \omega_3 = 0$. To remove the resonant forcing terms on the rhs of Eq. (9), it can be shown that the time evolution of the three wave amplitudes must follow (see Pedlosky 1987):

$$\frac{da_1}{dt} + \frac{B(K_2, K_3)}{K_1^2 + F} a_2 a_3 = 0, \quad (11) \quad a_2 = A_2 + \alpha_2(t), \quad a_1 = \alpha_1(t), \quad \text{and} \quad a_3 = \alpha_3(t), \quad (15)$$

$$\frac{da_2}{dt} + \frac{B(K_3, K_1)}{K_2^2 + F} a_3 a_1 = 0, \quad \text{and} \quad (12)$$

$$\frac{da_3}{dt} + \frac{B(K_1, K_2)}{K_3^2 + F} a_1 a_2 = 0. \quad (13)$$

Physically, Eqs. (11)–(13) dictate the energy exchanges among the three baroclinic waves introduced at the outset in Eq. (8).

In the following, we will apply the above triad wave interaction theory to gain insight into the numerical model results presented in the preceding section. As illustrated in Fig. 8b, the large-scale wind forcing generates the annual baroclinic Rossby waves, so, without loss of generality, let us assume they have the form

$$\psi_0 = A_2 \cos(k_2 x + l_2 y - \omega_2 t), \quad (14)$$

where the wave amplitude A_2 depends on the magnitude of the wind forcing, $\omega_2 = 2\pi/1$ yr, and l_2 is initially zero at the meridionally aligned eastern boundary. Given the dispersion relation Eq. (6), we can determine the ray paths of these annual waves emanating from the eastern boundary using the ray theory of Schopf et al. (1981); see Fig. 13a. Notice that along a ray path, k_2 and ω_2 are constant because the model background–mean state is invariant in time and longitude and l_2 increases owing to the decreasing F toward lower latitude. This change in l_2 is illustrated in Figs. 13b and 13c by the wavenumber vectors (k_2, l_2) along the ray path initiated at 20°N, 1 versus 2 yr west of the eastern boundary (i.e., at locations A and B in Fig. 13a).

Once the wind-forced annual Rossby wave (to be called the primary wave below) leaves the eastern boundary, it will be perturbed by secondary baroclinic Rossby waves that satisfy the resonant conditions (10). The dots in Figs. 13b and 13c indicate the possible secondary waves that meet the resonant conditions at locations A and B, respectively. Constrained by the conservation of energy and enstrophy, however, only those secondary waves that satisfy $K_1 < K_2 < K_3$ are able to extract energy from the primary wave and result in triad instability. In Figs. 13b and 13c, these instability-generating waves are marked by the nonblack dots; specifically, the “long” secondary waves (k_1, l_1) appear in the first quadrant inside the circle of radius = K_2 and the “short” secondary waves (k_3, l_3) appear in the fourth quadrant outside of the circle.

For the instability-generating secondary waves, their growth rate can be quantified by letting

in which the primary wave amplitude A_2 is given in Eq. (14). Assuming $\alpha_j(t) \ll A_2$ ($j = 1, 2, 3$), it is easy to prove using Eqs. (11) and (13) that the exponential growth rate for the secondary waves is given by

$$\lambda = A_2 \left[\frac{B(K_2, K_3)B(K_1, K_2)}{(K_1^2 + F)(K_3^2 + F)} \right]^{1/2}. \quad (16)$$

Notice that λ is proportional to A_2 , the streamfunction amplitude of the wind-driven primary wave. In Figs. 13b and 13c, we indicate the λ/A_2 ratio in color for the instability-generating secondary waves. As in other instability problems, the most unstable secondary wave will dominate the evolution of the unstable eddy field and the eddy’s meridional scales in this case will be determined by the wavelength $2\pi/l_3$.

By evaluating the secondary wave properties at all points along the ray paths of the annual baroclinic Rossby waves, we plot in Figs. 14a and 14b the spatial distributions of λ/A_2 and $2\pi/l_3$ of the most unstable “short” secondary waves. By and large, the growth rate increases and the meridional wavelength decreases westward, suggesting that the triad interaction tends to be progressively more intense, and dominated by smaller-scale eddies, when the primary wave propagates farther to the west. In reality, as shown in Fig. 8b, the primary waves will break down before entering the western region of more intense triad interactions. Physically, we can expect the breakdown of the primary waves to occur where the e -folding time scale of the triad instability, that is, λ^{-1} , matches the advective time scale of the primary wave, $(2\pi/K_2)/c_g$, where $c_g = [(\partial\omega_2/\partial k_2)^2 + (\partial\omega_2/\partial l_2)^2]^{1/2}$ is the speed of group velocity of the primary wave. If $\lambda^{-1} > (2\pi/K_2)/c_g$, the secondary waves will not have sufficient time to extract energy from the primary wave before the properties of the interacting waves alter along the primary wave’s ray paths.

Using the values presented in Fig. 14, we plot by black and white curves in Fig. 15 and Fig. 14b the locations where $\lambda^{-1} = (2\pi/K_2)/c_g$ for the three model runs in which the wind forcing amplitude W_0 is (a) 0.042, (b) 0.021, and (c) 0.0105 N m^{-2} , respectively (recall Figs. 8a, 12a, and 12b). From the model ULT field, the wind-induced primary waves in these three cases have an initial streamfunction amplitude of $A_2 = (g'/f) \times 100$ m, $(g'/f) \times 50$ m, and $(g'/f) \times 25$ m, respectively. Also plotted in Fig. 15 are the time-mean zonal flows, or where the nonlinear eddies are, in the three model runs. It is clear that the balance of $\lambda^{-1} = (2\pi/K_2)/c_g$ reasonably

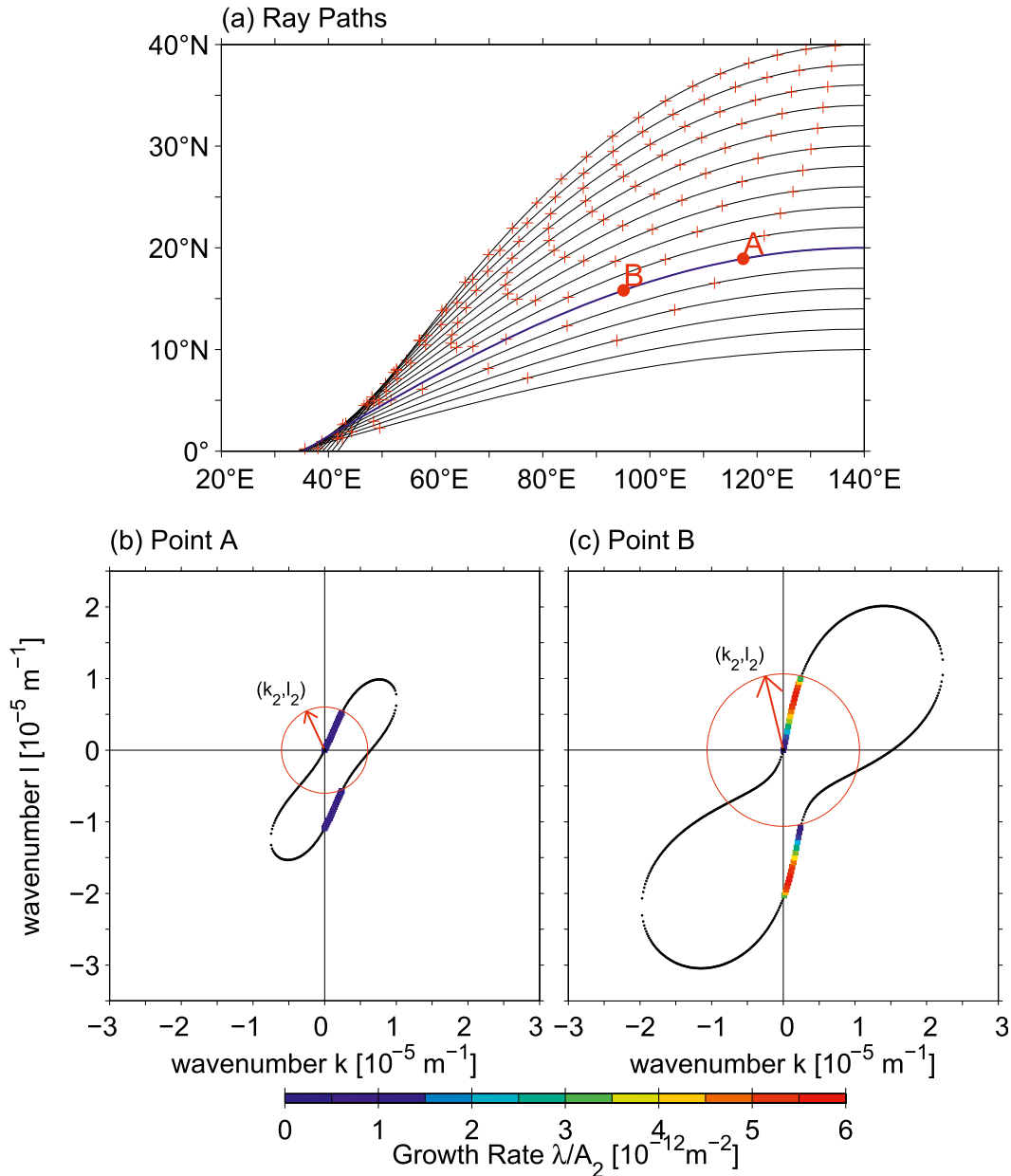


FIG. 13. (a) Ray paths for the annual baroclinic Rossby waves emanating from a meridionally aligned eastern boundary. Pluses indicate the time (yr) along each path. (b) Vector (k_2, l_2) denotes the primary annual Rossby wave at location A shown in (a). Discrete dots denote all secondary waves that satisfy the triad conditions [Eq. (10)]. The nonblack dots denote those secondary waves that are resonantly unstable with colors indicate the growth rate λ/A_2 defined in Eq. (16). (c) As in (b), but for location B shown in (a).

predicts where the primary waves will breakdown because of the triad instability.

In addition to identifying the breakdown locations of the primary waves, $\lambda^{-1} = (2\pi/K_2)/c_g$ also provides a measure for evaluating the meridional scale of the eddies responsible for generating the time-mean zonal jets. Specifically, based on the white curves in Fig. 14b, the meridional wavelengths $2\pi/l_3$ averaged along the

$\lambda^{-1} = (2\pi/K_2)/c_g$ locations are about 490, 350, and 270 km, respectively.² These theoretically predicted values agree favorably with the wavelengths (about

² Variations in $2\pi/l_3$ along the $\lambda^{-1} = (2\pi/K_2)/c_g$ curves are relatively small, less than 20% of the along-curve-mean values.

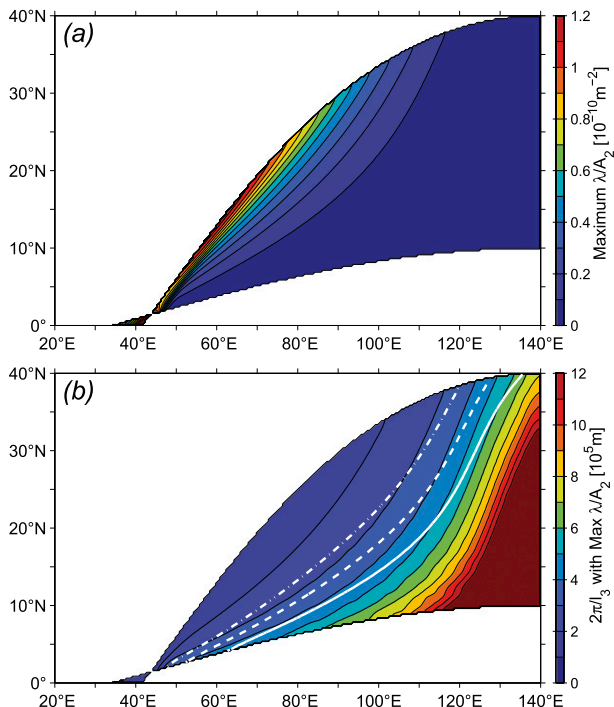


FIG. 14. (a) Distribution of growth rate λ/A_2 for the most unstable secondary waves along the primary Rossby wave ray paths. (b) Distribution of meridional wavelength $2\pi/l_3$ for the most unstable “short” secondary wave along the primary Rossby wave ray paths. White solid, dashed, and chain lines denote the locations where the e -folding time scale of the most unstable triad instability λ^{-1} matches the advective time scale of the primary wave $(2\pi/K_2)/c_g$ with $A_2 = (g'/f) \times 100$ m, $(g'/f) \times 50$ m, and $(g'/f) \times 25$ m, respectively.

500, 360, and 280 km) estimated directly from the modeled time-mean zonal flows.

Regarding the breakdown of wind-forced baroclinic Rossby waves, we note that the recent studies by LaCasce and Pedlosky (2004) and Zhang and Pedlosky (2007) have considered their triad interactions with a baroclinic secondary wave and a third barotropic secondary Rossby wave in the context of instability of Rossby basin modes. Their notion that a critical parameter for wave breakdown exists, given by the ratio of the transit time of long Rossby wave to the e -folding time of triad instability, is conceptually similar to the $\lambda^{-1} = (2\pi/K_3)/c_g$ threshold considered in this study.

In closing this section, we briefly comment on the effect of horizontal eddy viscosity. As formulated in detail in the appendix, it is mathematically straightforward to add the horizontal eddy viscosity term to the QG potential vorticity equation. Following the same procedures put forth earlier in this section, we can find the exponential growth rate λ for the secondary waves in the presence of eddy viscosity by solving the quadratic equation:

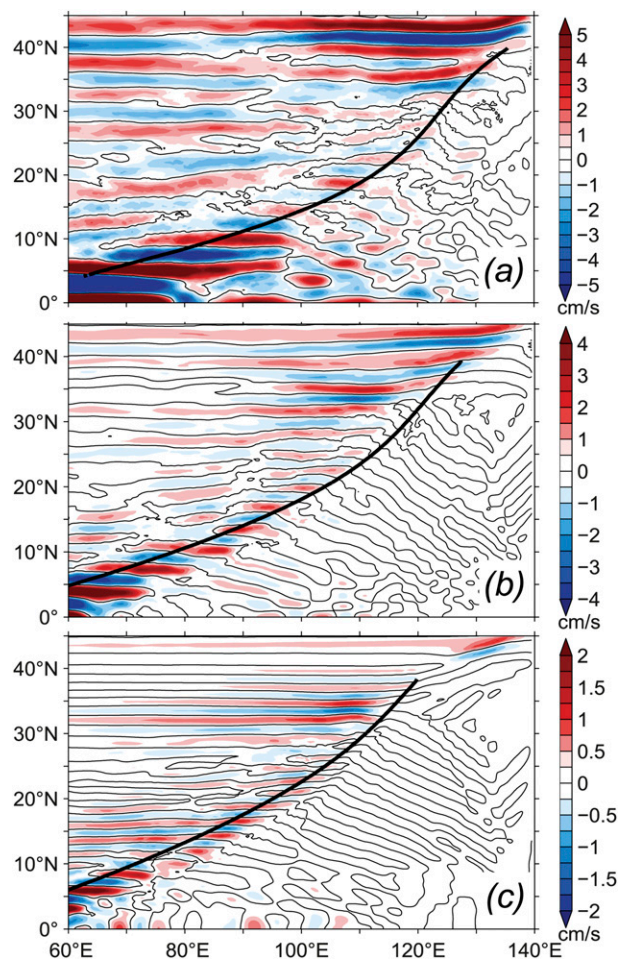


FIG. 15. (a) Solid black line demarcates the location for the base model run where the e -folding time scale of the most unstable triad instability matches the advective time scale of the primary wave. Contours show the modeled time-mean zonal velocity (same as in Fig. 8a). (b) As in (a), but for the half-amplitude forcing run (Fig. 12a). (c) As in (a), but for the quarter-amplitude forcing run (Fig. 12b).

$$\lambda^2 + A_h \left(\frac{K_1^4}{K_1^2 + F} + \frac{K_3^4}{K_3^2 + F} \right) \lambda + \frac{A_h^2 K_1^4 K_3^4 - B(K_2, K_3) B(K_1, K_2) A_2^2}{(K_1^2 + F)(K_3^2 + F)} = 0 \quad (17)$$

[see Eq. (A6) in the appendix]. In the inviscid limit of $A_h = 0$, Eq. (17) reduces to Eq. (16). Figure 16a shows the λ/A_2 of the most unstable secondary waves along 15°N when A_h is varied from 0 to $500 \text{ m}^2 \text{ s}^{-1}$. By definition, the λ/A_2 value at $A_h = 0$ matches that shown in Fig. 14a along 15°N . Within this A_h value range, there is minimal impact on the growth rate of the most unstable secondary waves owing to the changing eddy viscosity.

This insensitivity of λ on the A_h value also means that the meridional wavelength $2\pi/l_3$ for the most unstable

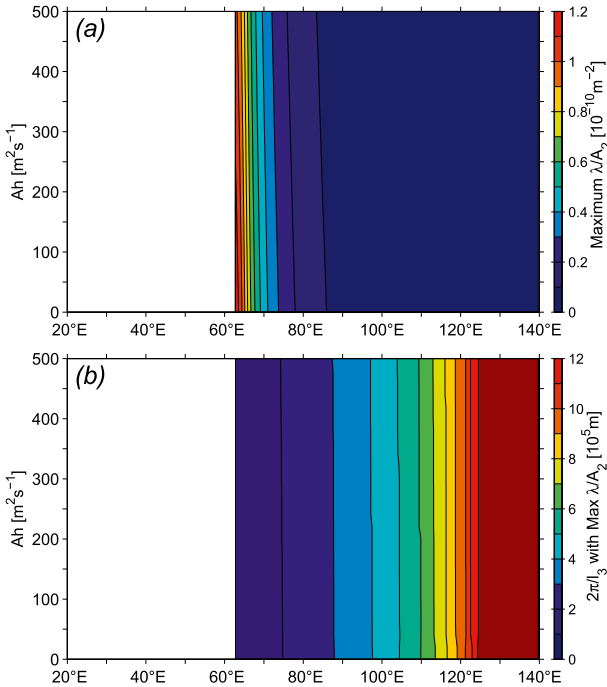


FIG. 16. (a) Growth rate λ/A_2 for the most unstable secondary waves along 15°N as a function of A_h . (b) Meridional wavelength $2\pi/l_3$ for the most unstable “short” secondary wave along 15°N as a function of A_h . At $A_h = 0$, both the λ/A_2 and $2\pi/l_3$ values reduce to those along 15°N shown in Figs. 14a and 14b, respectively.

secondary wave remains largely independent of the A_h value (see Fig. 16b). This last result explains why the time-mean zonal jets in the model runs with $A_h = 100\text{ m}^2\text{ s}^{-1}$ and $200\text{ m}^2\text{ s}^{-1}$ have a similar meridional wavelength as the base model run with $A_h = 20\text{ m}^2\text{ s}^{-1}$ (cf. Figs. 8a and 11).

5. Eddy-driven zonal-mean jets

After the nonlinear triad interactions, the wind-driven annual baroclinic Rossby waves break down, generating isolated mesoscale eddies (recall Figs. 8b and 9). As these nonlinear eddies propagate westward, they interact and are able to induce time-mean zonal jets through, again, nonlinear interactions. To quantify the effect of the nonlinear eddies in forming the time-mean circulation, it is useful to diagnose the potential vorticity budget. For the $1\frac{1}{2}$ -layer reduced-gravity model governed by Eqs. (2)–(3), it is straightforward to show that potential vorticity $Q = (f + \mathbf{k} \cdot \nabla \times \mathbf{u})/H$ is Lagrangianly conserved; that is, $DQ/Dt = 0$, in the unforced and inviscid limit. By decomposing all variables a into $a = \bar{a} + a'$, where the overbar indicates temporal averaging and the prime indicates the deviation from the time mean, we have

$$\bar{\mathbf{u}} \cdot \nabla \bar{Q} = -\overline{\mathbf{u}' \cdot \nabla Q'}. \quad (18)$$

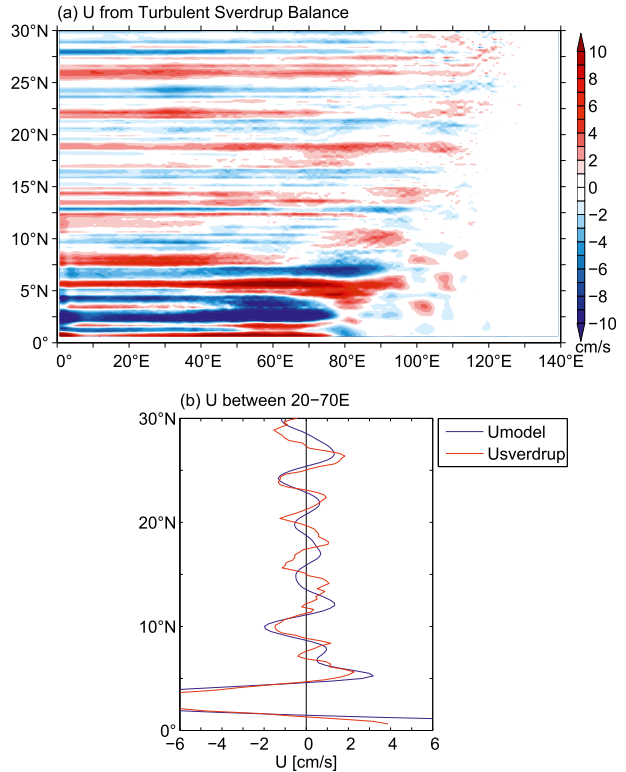


FIG. 17. (a) Zonal time-mean velocity calculated from the turbulent Sverdrup balance in the base model run. (b) Comparison of the zonal time-mean velocity averaged over $20^\circ\text{--}70^\circ\text{E}$ from the base model run (blue) vs from the turbulent Sverdrup balance (red).

In the cases considered in this study, $\partial \bar{Q} / \partial x$ is nearly zero and, as such, $\bar{\mathbf{u}} \cdot \nabla \bar{Q} \approx \bar{v} \partial \bar{Q} / \partial y$. Known as the turbulent Sverdrup balance (Rhines and Holland 1979), Eq. (18) relates the convergence of eddy potential vorticity fluxes to the mean flow across the mean potential vorticity gradient. Once $\bar{v}(x, y)$ is determined using Eq. (18), the mean zonal flow $\bar{u}(x, y)$ can be calculated from the time-mean continuity equation:

$$\bar{u}(x, y) = -\frac{1}{H} \int_{x_e}^x \frac{\partial}{\partial y} (\bar{H} \bar{v}) dx, \quad (19)$$

where x_e denotes the eastern boundary.

Using the \mathbf{u}' and H' data from the base model run (i.e., Fig. 8) with primes here denoting the deviations from the last 10-yr model-mean field, we plot in Fig. 17a the $\bar{u}(x, y)$ field evaluated using Eqs. (18)–(19). Notice that the time-mean zonal flow is nearly zero close to the eastern boundary, a feature seen also in Fig. 8a. This is because the wind-driven annual baroclinic Rossby waves are largely linear in nature, producing as a result no rectified mean flows. Reflecting the dominance of β effect, the eddy-driven flows west of the breakdown boundary of the annual Rossby waves appear zonally coherent. Averaging

over the 20°–70°E zonal band, the zonal jets derived from Eqs. (18)–(19) (red curve in Fig. 17b) agree well with the time-mean zonal jets calculated directly from the base case model output (blue curve in Fig. 17b). In other words, the time-mean zonal jets detected west of the breakdown boundary of the annual baroclinic Rossby waves are due to the potential vorticity flux convergence of the nonlinear eddies generated through the triad instability.

Both the blue and red curves in Fig. 17b indicate the presence of an eastward time-mean zonal jet along the equator. Generation of this equatorial eastward jet can be heuristically understood as follows. When the annually varying wind stress $\tau^x(0, t)$ in Eq. (4) is positive along the equator, a positive u' is generated along the equatorial band. Since $\tau^x(0, t) > 0$ induces negative (positive) v' to the north (south) of the equator through Ekman convergence, this results in $\partial(u'v')/\partial y < 0$ along the equatorial band. When the annually varying $\tau^x(0, t)$ forcing switches to negative, the along-equator u' becomes negative and Ekman divergence causes a positive v' north of the equator and a negative v' south of the equator. This, again, results in an eastward momentum flux convergence $\partial(u'v')/\partial y < 0$. With $\partial(u'v')/\partial y < 0$, an eastward time-mean jet is induced along the equator as shown in Fig. 17b. Notice that, once the zonal jet direction is set at the equator, the latitudinal positions of the off-equatorial eastward jets are determined by the meridional wavelength $2\pi/l_3$ along the Rossby wave breakdown boundary (recall the white curves in Fig. 14b). In the 1/2-layer model run of Fig. 10a, for example, $2\pi/l_3 \simeq 500$ km and the eastward zonal jets appear near 5°, 9°, 14°N and so on. In the realistic western North Pacific basin, no time-mean jets appear north of 22°N (see Figs. 1 and 2) because the Hawaiian archipelago blocks the westward propagation of the breakdown eddies.

6. Summary

By means of numerical modeling and theoretical examinations, we have in this study explored the formation mechanisms for the recently identified North Equatorial Undercurrent (NEUC) jets in the tropical North Pacific Ocean. Present from the western boundary to about 120°W, the NEUC jets are detected to exist zonally coherently along approximately 9°, 13°, and 18°N. These characteristics of the observed time-mean NEUC jets are favorably captured in the multidecadal hindcast simulations of the eddy-resolving OFES model. Using the OFES hindcast simulation output, we investigated the time-varying signals of the NEUC jets and detected that they are temporally quasi-permanent over the past six decades and exhibit the mode-1 baroclinic vertical structure. An examination into the OFES rms velocity

signals on the core layer of the NEUC jets further revealed that a southwest–northeast tilting boundary exists in the eastern Pacific basin, west of which the velocity variance is significantly elevated.

Based on these time-varying features of the NEUC jets in the OFES simulations, we adopted a nonlinear 1/2-layer reduced-gravity model so as to unravel the relevant physical processes underlying the NEUC jet formation. By forcing the model with the annually varying wind stresses that mimic the large-scale Pacific Ocean wind field, we found that the nonlinear mode-1 baroclinic processes capture the essential dynamics of the NEUC jet generation. Specifically, the modeled time-mean zonal jets have a meridional wavelength of ~ 500 km similar to the observations, and like in the OFES simulation, there exists a southwest–northeast tilting boundary that separates the high-variance western basin from the low-variance eastern basin. Dynamically, this tilting boundary signifies where these wind-forced Rossby waves break down and form isolated nonlinear eddies. By diagnosing the eddy potential vorticity budget, we found that the time-mean zonal jets formed west of the tilting boundary are due to the eddy potential vorticity flux convergence through the turbulent Sverdrup balance.

Simplicity of the 1/2-layer reduced-gravity mechanism allowed us to theoretically clarify the breakdown process for the wind-forced annual baroclinic Rossby waves. By regarding the wind-forced Rossby wave emanating from the eastern boundary as a primary wave, we found that it interacts with secondary baroclinic Rossby waves that satisfy the triad conditions. Although unstable triad interactions are always existent, their growth rate near the eastern boundary is usually small, disallowing the primary wave to break down before the interacting waves change their properties along the ray paths. As the wind-forced primary wave propagates away from the eastern boundary, its meridional wavenumber increases as does the growth rate of the possible triad instability. Our model experiments showed that the wind-forced, primary waves break down where the e -folding time scale of the most unstable triad instability matches the advective time scale of the primary wave. The meridional wavelength of the most unstable “short” secondary wave not only determines the length scale of the breakdown mesoscale eddies, it also controls the wavelength of the eddy-induced, time-mean, zonal jets.

The triad interaction theory reveals that the growth rate of the triad instability is proportional to the amplitude of wind-forced primary waves. As a result, a larger-amplitude primary wave tends to succumb to the triad instability closer to the eastern boundary, generating broader-scale mesoscale eddies and wider resultant time-mean zonal jets. This result was confirmed in our model

runs in which the applied wind forcing amplitude was varied parametrically. While dominating in the eastern Pacific basin, the annual-period surface wind forcing does change in its amplitude on interannual and longer time scales. This dependence of the zonal jet's meridional scale on the amplitude of the external wind forcing, may explain some of the interannual changes in the NEUC jets detected in the long-term OFES simulations (recall Fig. 3).

Although we have focused on the Northern Hemisphere zonal jet features throughout this study, our idealized model results, such as those presented in Fig. 8, are symmetrically valid with respect to the equator for the Southern Hemisphere. Using a coupled atmosphere–ocean general circulation model, Taguchi et al. (2012) have recently found subthermocline zonal jets existing in the tropical central South Pacific Ocean. In accordance with the analysis by Kessler and Gourdeau (2006), Taguchi et al. (2012) demonstrated that these zonal jets are in approximate Sverdrup balance with the collocated, small-scale, surface wind stress curl forcing. A look at the observed zonal jet structures shown in Fig. 2d of Taguchi et al. (2012) reveals that there exist six eastward jets between 5° and 32°S with roughly equal spacing. The geographical locations of these observed eastward jets agree very favorably with the modeled eastward jets shown in Fig. 8a (assuming equatorial symmetry). Given this agreement, we suggest that, like the NEUC jets, the eastward jets observed in the tropical South Pacific Ocean are also generated by nonlinear eddies as a result of breakdown of the wind-forced annual baroclinic Rossby waves owing to triad instability. By affecting the sea surface temperatures and overlying small-scale wind stress curl field (Taguchi et al. 2012), the eddy-induced zonal jets are further enhanced by the small-scale wind stress curls through the linear Sverdrup dynamics.

Using a barotropic quasigeostrophic model, Wang et al. (2012) have recently shown that quasi-zonal jets can be generated by radiating barotropic instability of an unstable eastern boundary current. Although the eastern boundary plays an important role in forming westward-propagating baroclinic Rossby waves in this study, our proposed zonal jet formation mechanism (i.e., the triad instability of the baroclinic Rossby waves) is fundamentally different from the eastern boundary current instability mechanism considered by Wang et al.

Taking the process-oriented modeling approach, we have in this study intentionally excluded the influence of the large-scale circulation driven by the time-mean wind stress curl forcing (e.g., the westward NEC). Both float observations and the OFES simulation reveal that the NEUC jets slant weakly in the southwest–northeast direction (Figs. 1 and 2) and we expect this slanting to be caused by the nonzonal-mean potential vorticity gradient

field modified by the presence of the time-mean wind-driven circulation. It will be interesting for future studies to quantify how inclusion of the time-mean wind forcing to Eq. (4) modifies the annual baroclinic Rossby waves, their triad instability, and their subsequent breakdown and formation of multiple cross-basin zonal jets.

Acknowledgments. This study benefitted from discussions with Francois Ascani, Eric Firing, Richard Greatbatch, Billy Kessler, Roger Lukas, Jay McCreary, Peter Rhines, Dan Rudnick, Bunmei Taguchi, and Yu Zhang. We thank the anonymous reviewers whose detailed comments helped improve an early version of the manuscript. The Argo profiling float data used in this study were provided by the US-GODAE Argo Global Data Assembly Center. This study was supported by the ONR project Origins of the Kuroshio and Mindanao Current (OKMC), N00014-10-1-0267.

APPENDIX

Effect of Horizontal Eddy Viscosity on Secondary Wave Growth Rate

When the horizontal eddy viscosity effect is present, the QG potential vorticity Eq. (5) can be rewritten as

$$\frac{\partial}{\partial t}(\nabla^2\psi - F\psi) + J(\psi, \nabla^2\psi) + \beta \frac{\partial\psi}{\partial x} = A_h \nabla^4\psi, \quad (\text{A1})$$

where A_h is the horizontal eddy viscosity coefficient, a quantity also used in Eq. (2). Like the nonlinear Jacobian term, the eddy viscosity term can be similarly assumed to operate at $O(\epsilon)$ and Eq. (9) in this case modifies to

$$\begin{aligned} \frac{\partial}{\partial t}(\nabla^2\psi_1 - F\psi_1) + \beta \frac{\partial\psi_1}{\partial x} &= -J(\psi_0, \nabla^2\psi_0) + A_h \nabla^4\psi_0 \\ &= \sum_{m=1}^3 \sum_{n=1}^3 \frac{a_m a_n}{2} B(K_m, K_n) [\cos(\theta_m + \theta_n) \\ &\quad - \cos(\theta_m - \theta_n)] + \sum_{m=1}^3 A_h K_m^4 a_m \cos\theta_m. \end{aligned} \quad (\text{A2})$$

Inclusion of the A_h term does not alter the triad conditions [Eq. (10)], but it changes Eqs. (11)–(13) that govern the wave amplitude evolution to

$$\frac{da_1}{dt} + \frac{B(K_2, K_3)}{K_1^2 + F} a_2 a_3 + A_h \frac{K_1^4}{K_1^2 + F} a_1 = 0, \quad (\text{A3})$$

$$\frac{da_2}{dt} + \frac{B(K_3, K_1)}{K_2^2 + F} a_1 a_3 + A_h \frac{K_2^4}{K_2^2 + F} a_2 = 0, \quad \text{and} \quad (\text{A4})$$

$$\frac{da_3}{dt} + \frac{B(K_1, K_2)}{K_3^2 + F} a_2 a_1 + A_h \frac{K_3^4}{K_3^2 + F} a_3 = 0. \quad (\text{A5})$$

By adopting Eq. (15) for the time-varying primary and secondary wave amplitudes and using Eqs. (A3) and (A5), we can derive the exponential grow rate λ for the secondary waves by solving

$$\lambda^2 + A_h \left(\frac{K_1^4}{K_1^2 + F} + \frac{K_3^4}{K_3^2 + F} \right) \lambda + \frac{A_h^2 K_1^4 K_3^4 - B(K_2, K_3) B(K_1, K_2) A_2^2}{(K_1^2 + F)(K_3^2 + F)} = 0. \quad (\text{A6})$$

REFERENCES

- Ascani, F., E. Firing, P. Dutrieux, J. P. McCreary, and A. Ishida, 2010: Deep equatorial ocean circulation induced by a forced-dissipated Yanai beam. *J. Phys. Oceanogr.*, **40**, 1118–1142.
- Berloff, P., I. Kamenkovich, and J. Pedlosky, 2009: A model of multiple zonal jets in the oceans: Dynamical and kinematical analysis. *J. Phys. Oceanogr.*, **39**, 2711–2734.
- Chelton, D. B., M. G. Schlax, and R. M. Samelson, 2011: Global observations of nonlinear mesoscale eddies. *Prog. Oceanogr.*, **91**, 167–216.
- Cravatte, S., W. S. Kessler, and F. Marin, 2012: Intermediate zonal jets in the tropical Pacific Ocean observed by Argo floats. *J. Phys. Oceanogr.*, **42**, 1475–1485.
- Ducet, N., P.-Y. Le Traon, and G. Reverdin, 2000: Global high-resolution mapping of ocean circulation from TOPEX/Poseidon and ERS-1 and -2. *J. Geophys. Res.*, **105**, 19477–19498.
- Dutrieux, P., 2009: Tropical western Pacific currents and the origin of intraseasonal variability below the thermocline. Ph.D. thesis, University of Hawaii at Manoa, 122 pp.
- Hu, D., and M. Cui, 1991: The western boundary current of the Pacific and its role in the climate. *Chin. J. Oceanology Limnol.*, **9**, 1–14.
- Kamenkovich, I., P. Berloff, and J. Pedlosky, 2009: Roles of eddy forcing in the dynamics of multiple zonal jets in a model of the North Atlantic. *J. Phys. Oceanogr.*, **39**, 1361–1379.
- Kashino, Y., N. Espana, F. Syamsudin, K. J. Richards, T. Jensen, P. Dutrieux, and A. Ishida, 2009: Observations of the North Equatorial Current, Mindanao Current, and the Kuroshio Current system during the 2006/07 El Niño and 2007/08 La Niña. *J. Oceanogr.*, **65**, 325–333.
- Kessler, W. S., and L. Gourdeau, 2006: Wind-driven zonal jets in the South Pacific Ocean. *Geophys. Res. Lett.*, **33**, L03608, doi:10.1029/2005GL025084.
- Kistler, R., and Coauthors, 2001: The NCEP–NCAR 50-Year Reanalysis: Monthly means CD-ROM and documentation. *Bull. Amer. Meteor. Soc.*, **82**, 247–267.
- LaCasce, J. H., and J. Pedlosky, 2004: The instability of Rossby basin modes and the oceanic eddy field. *J. Phys. Oceanogr.*, **34**, 2027–2041.
- Maximenko, N. A., B. Bang, and H. Sasaki, 2005: Observational evidence of alternating zonal jets in the world ocean. *Geophys. Res. Lett.*, **32**, L12607, doi:10.1029/2005GL022728.
- Nakano, H., and H. Hasumi, 2005: A series of zonal jets embedded in the broad zonal flows in the Pacific obtained in eddy-permitting ocean general circulation models. *J. Phys. Oceanogr.*, **35**, 474–488.
- Nonaka, M., H. Nakamura, Y. Tanimoto, T. Kagimoto, and H. Sasaki, 2006: Decadal variability in the Kuroshio–Oyashio Extension simulated in an eddy-resolving OGCM. *J. Climate*, **19**, 1970–1989.
- Ollitrault, M., M. Lankhorst, D. Fratantoni, P. Richardson, and W. Zenk, 2006: Zonal intermediate currents in the equatorial Atlantic Ocean. *Geophys. Res. Lett.*, **33**, L05605, doi:10.1029/2005GL025368.
- Pedlosky, J., 1987: *Geophysical Fluid Dynamics*. Springer-Verlag, 710 pp.
- Qiu, B., 1999: Seasonal eddy field modulation of the North Pacific Subtropical Countercurrent: TOPEX/Poseidon observations and theory. *J. Phys. Oceanogr.*, **29**, 2471–2486.
- , and T. M. Joyce, 1992: Interannual variability in the mid- and low-latitude western North Pacific. *J. Phys. Oceanogr.*, **22**, 1062–1079.
- , and S. Chen, 2012: Multidecadal sea level and gyre circulation variability in the northwestern tropical Pacific Ocean. *J. Phys. Oceanogr.*, **42**, 193–206.
- , D. L. Rudnick, S. Chen, and Y. Kashino, 2013: Quasi-stationary North Equatorial Undercurrent jets across the tropical North Pacific Ocean. *Geophys. Res. Lett.*, **40**, 2183–2187, doi:10.1002/grl.50394.
- Rhines, P. B., 1975: Waves and turbulence on a beta-plane. *J. Fluid Mech.*, **69**, 417–443.
- , and W. R. Holland, 1979: A theoretical discussion of eddy-driven mean flows. *Dyn. Atmos. Oceans*, **3**, 289–325.
- Richards, K. J., N. A. Maximenko, F. O. Bryan, and H. Sasaki, 2006: Zonal jets in the Pacific Ocean. *Geophys. Res. Lett.*, **33**, L03605, doi:10.1029/2005GL024645.
- Roemmich, D., and Coauthors, 2009: The Argo program: Observing the global ocean with profiling floats. *Oceanography*, **22**, 34–43.
- Sasaki, H., M. Nonaka, Y. Masumoto, Y. Sasai, H. Uehara, and H. Sakuma, 2008: An eddy-resolving hindcast simulation of the quasi-global ocean from 1950 to 2003 on the Earth Simulator. *High Resolution Numerical Modelling of the Atmosphere and Ocean*, W. Ohfuchi and K. Hamilton, Eds., Springer, 157–185.
- Schopf, P. S., D. L. T. Anderson, and R. Smith, 1981: Beta-dispersion of low-frequency Rossby waves. *Dyn. Atmos. Oceans*, **5**, 187–214.
- Taguchi, B., R. Furue, N. Komori, A. Kuwano-Yoshida, M. Nonaka, H. Sasaki, and W. Ohfuchi, 2012: Deep oceanic zonal jets constrained by fine-scale wind stress curls in the South Pacific Ocean: A high-resolution coupled GCM study. *Geophys. Res. Lett.*, **39**, L08602, doi:10.1029/2012GL051248.
- Tailleux, R., and J. C. McWilliams, 2001: The effect of bottom pressure decoupling on the speed of extratropical, baroclinic Rossby waves. *J. Phys. Oceanogr.*, **31**, 1461–1476.
- Toole, J. M., E. Zou, and R. C. Millard, 1988: On the circulation of the upper waters in the western equatorial Pacific Ocean. *Deep-Sea Res.*, **35**, 1451–1482.
- Wang, F., D. Hu, and H. Bai, 1998: Western boundary undercurrents east of the Philippines. *Proc. Fourth Pacific Ocean Remote Sensing Conference (PORSEC)*, Qingdao, China, PORSEC, 551–556.
- Wang, J., M. A. Spall, G. R. Flierl, and P. Malanotte-Rizzoli, 2012: A new mechanism for the generation of quasi-zonal jets in the ocean. *Geophys. Res. Lett.*, **39**, L10601, doi:10.1029/2012GL051861.
- Wyrtki, K., and B. Kilonsky, 1984: Mean water and current structure during the Hawaii-to-Tahiti shuttle experiment. *J. Phys. Oceanogr.*, **14**, 242–254.
- Zhang, Y., and J. Pedlosky, 2007: Triad instability of planetary Rossby waves. *J. Phys. Oceanogr.*, **37**, 2158–2171.